

The following publication Meng, Q., & Hsu, L. T. (2020). Integrity Monitoring for All-Source Navigation Enhanced by Kalman Filter-Based Solution Separation. IEEE Sensors Journal, 21(14), 15469-15484 is available at <https://doi.org/10.1109/JSEN.2020.3026081>

Integrity Monitoring for All-Source Navigation Enhanced by Kalman Filter based Solution Separation

Qian Meng and Li-Ta Hsu

Abstract—Integrity is a popular and effective index as a measure of trust for navigation system to place in the correct position. The classical snapshot-based integrity monitoring methods have a widely and mature application in global navigation satellite system (GNSS) assessment. However, they cannot meet the integrity evaluation requirements for multi-sensor integration such as all-source navigation due to its recursive estimation and measurement diversity of sensors, which directly limits its use in safety-critical applications. We propose a new Kalman filter based solution separation (KFSS) method for the integrity monitoring of multi-sensor integrated navigation systems. The traditional EKF update estimation is remodeled as a weighted least square form to involve the system propagation into the new measurement vector, which reconstructed as a ‘pseudo-snapshot’ model. The integrity risk caused by the system propagation is considered as one fault hypothesis in the following fault detection and protection level determination. Then, the integrity evaluation is executed in positioning domain enhanced by solution separation with sensor exclusion. The above two operations have indispensable roles and inseparable relationship from the aspect of integrity functional realization. The performance of a tightly coupled integration simulation, a loosely coupled multi-sensor integration simulation and an actual kinematic vehicle experiment verified the feasibility and superiority of the proposed method. The KFSS structure can detect fault in propagation period and step fault, ramp fault and simultaneous faults in observations effectively. The protection levels can be reduced positively both in horizontal and vertical directions, which is positive to bound the position error more accurately and reduce the redundant space effectively. It is of great significance for tighter integrity requirements.

Index Terms—Integrity monitoring, Kalman filter, Loosely couple, All-source navigation, Solution separation, Tightly couple

I. INTRODUCTION

MULTI-SENSOR navigation integration technology, which shows superiority in accuracy and reliability, is the major research direction in navigation and positioning. It is also a basic implementation technology for the all-source navigation, resilient sensor management and other advanced navigation structures [1,2,3]. Based on its redundant measurement information, multi-sensor integration is also

widely used in safety-critical applications such as civil aviation, autonomous vehicles, pedestrian navigation, smart grid and intelligent transportation system [4,5,6,7]. However, with more sensors and observations involved in the navigation system, the probability of faults and outliers is increased simultaneously. The sensor-agnostic performance and availability in different scenarios are also uncertainties affecting the multi-sensor navigation results.

For evaluating the impact of sensor measurements on the positioning results, integrity is a representative quantifiable criterion which has been introduced and researched in many fields. Different from the traditional fault detection technology, integrity puts more emphasis on the measure of trust that can be placed in the correct position and the ability to provide timely alert when the navigation system should not be used for navigation [8]. Integrity was firstly introduced in satellite navigation and accepted by the civil aviation as one of the crucial criteria for satellite-based navigation system [9]. The classical integrity solution for global navigation satellite system (GNSS) is receiver autonomous integrity monitoring (RAIM), including residual detection method in range domain and solution separation method in positioning domain [10,11]. As the measurements are pseudoranges of satellites, most of the RAIM methods follow the snapshot principle which only use the absolute positioning measurements at the current epoch. However, in multi-sensor navigation system, the final positioning results are recursive solutions which integrated different types of measurements from all available sensors [12,13,14]. In most cases, the recursive solutions are implemented by an optimal estimator like extended Kalman filter (EKF) with sequential epochs [15,16,17]. The classical EKF includes two steps further: state propagation and measurements update. The traditional RAIM methods are not available for multi-sensor integration.

For the operation monitoring of multi-sensor integration, most of the researches focus on the fault detection and exclusion (FDE) function of inertial navigation system (INS) and GNSS integration. The operation of FDE is based on innovations or residuals of EKF, which cannot be defined as integrity monitoring strictly. In fact, only a few research works

This paragraph of the first footnote will contain the date on which you submitted your paper for review. This research is funded by the project “Security Enhancement of Positioning Sensors on Connected Autonomous

Vehicles” by Hong Kong Polytechnic University, grant number P0013910 (ZVP9). Corresponding author: Li-Ta Hsu

The Authors are with Hong Kong Polytechnic University (e-mail: qian2019.meng@polyu.edu.hk; lt.hsu@polyu.edu.hk).

mentioned the integrity for KF-based multi-sensor integration. [18] proposed a parallel KFs method to monitoring every measurement. However, the implementation is complex and the calculation burden is not optimistic. [19] introduced a residual based EKF integrity method and proved the test statistics chosen from the current and past time are independent. But the method adopted batch least-squares form of EKF, whose dimensions will explode with more sensors are involved. [20] proposed the resilient multi-sensor management concept but focused on the fault detection and sensor remodeling. [21] researched the integrity risk of EKF-based localization but the method is still based on residuals and dependent on the worst-case fault, which not considering the relevance of measurements from the same sensor. [22] extended the Advanced RAIM (ARAIM) method into INS/GNSS integration but the impact of state propagation on integrity risk is not considered. Besides what discussed above, the other works are mostly based on GNSS only or tightly coupled INS/GNSS integration, where the measurements are GNSS pseudoranges only and the methods cannot be extended to multi-sensor integration directly [23,24,25]. Furthermore, the integrity solution for loosely coupled multi-sensor integration is not considered in the literature.

Researchers are struggling to derive the impact of the temporal connectivity in the EKF in the calculation of the integrity risk. That is one of the current bottlenecks of obtaining the integrity for EKF-based sensor integration systems. If we can regard the system propagation as a measurement that containing the temporal connectivity of EKF, then we can have a chance to estimate the integrity of EKF. The state propagation and measurement update will be involved in one mapping function to share the integrity risk. In the other words, the new measurement model should comprise both system propagation and measurement update of the EKF. The problem is, how can we establish a new system model (mapping function) between the state and the new measurement model based on the information of the EKF of the integration system. In fact, the concept of extended RAIM proposed in [26] provided one embryonic form to establish this mapping function. The measurement update formula in classical EKF was remodeled as one least square form which included system propagation and measurement. However, its integrity scheme is still limited in INS/GNSS integration and cannot be extended to the all-sourced integrated navigation system. If we can extend the new measurement model to include all types of measurements of other sensors such as light detection and ranging (LiDAR) and visual-inertial navigation system (VINS) based on cameras, the idea can be used to establish a new framework to estimate the integrity of multi-sensors integrated system. This is the objective of this paper.

Furthermore, as shown in Fig. 1, for high accuracy application like autonomous driving, the multi-sensor navigation solution is the inevitable choice. However, LiDAR, cameras, GNSS and INS are providing different domains of measurements. The diversity of measurements and propagation of states make the integrity monitoring for KF-based multi-sensor integration another big challenge. Firstly, the

measurements are difficult to be evaluated in the same domain as some sensors provide range measurements while the other sensors only provide positioning results. The positioning results are further divided into absolute and relative values. Secondly, the measurements are not independent any longer [27]. In GNSS RAIM, one important hypothesis is that the pseudorange faults of satellites are independent [28]. But for LiDAR or visual simultaneous localization and mapping (SLAM), the measurements are interrelated which means one sensor fault may affect many measurements [29]. Standing at the point of view of the concept of solution separation, we can develop an integrity monitoring algorithm that can separate the sensors instead of the measurements inside a single sensor.

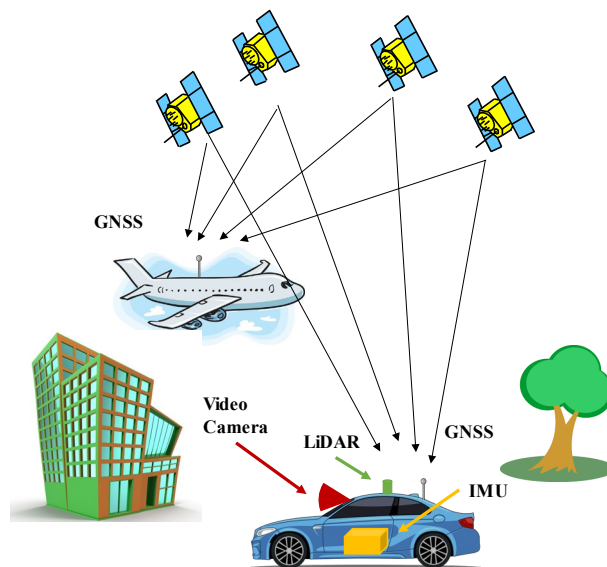


Fig. 1 Navigation sensor solutions for different applications. The circumstance for civil airplane is open, the GNSS navigation can meet the requirements in most case. However for autonomous driving, the surroundings are complex, and the safety space is extremely limited. High accuracy and reliable navigation solution is necessary.

This paper proposes a new Kalman filter based solution separation (KFSS) method to detect the fault of the sensors and further estimate the protection level of the navigation results. Firstly, the new system model is established with system propagation involved in integrity risk evaluation. Then, the state estimator can be written as a weighted least square form in preparation for solution separation. The equivalence between classical update estimation and weighted least square estimation is also given. Secondly, based on the weighted least square of EKF estimation, the solution separation is implemented in positioning domain with the function of fault detection and exclusion. Particularly the fault-tolerance position estimator is calculated with sensor exclusion. Finally, the protection levels are calculated with the integrity risk budget. The proposed method has no limitation in type and quantity of sensors, or the number of faults. The experiment simulation on tightly coupled integration and loosely coupled integration also verified the effectiveness of the proposed integrity method. The proposed method is well applicable for all-source navigation and resilient sensor management.

The contributions of this paper are summarized hereafter:

1) The least square form of EKF is introduced into integrity evaluation of multi-sensor integration. The weighted least square estimation is equivalent to the measurement update with Kalman gain. But the integrity risk produced by both the temporal connectivity and system propagation is considered in the integrity monitoring effectively. It results in that the integrity of the complex recursive estimation can be solved in a mature snapshot principle.

2) A solution separation with sensor exclusion is proposed. Due to the diversity and relevance of measurements, to detect and evaluate the fault based on residuals in range domain is difficult to be implemented. The solution separation with sensor exclusion make it clear and intuitive to analyze the impact of sensor fault to the multi-sensor estimator directly in positioning domain. The proposed method is well applicable to all-source navigation.

It is a fact that reform of EKF and solution separation have their different applications independently in the current research. But it should be noted that from the aspect of integrity monitoring, they have indispensable roles and inseparable relationship in functional realization. Reform of KF in this manuscript is to involve the integrity risk originated from the temporal connectivity and system propagation. Solution separation is to implement the FDE and protection level calculation in positioning domain with sensor exclusion, as it is difficult to operate in range domain due to the diversity and relevance of measurements.

II. WEIGHTED LEAST SQUARE FORM OF KALMAN FILTER FOR MULTI-SENSOR INTEGRATION

Based on the classical EKF, the least square form of system propagation and measurement update is given in this section. Then, we derive the weighted least square estimator with the measurement covariance and predicted error covariance and prove its equivalence with the EKF estimation with Kalman gain.

A. Kalman Filter with Least Square Form

For classical EKF, the propagation of the state can be written as

$$\mathbf{X}_k = \Phi \mathbf{X}_{k-1} + \mathbf{w}_k \quad (1).$$

where \mathbf{X}_{k-1} and \mathbf{X}_k are the updated state estimation at $(k-1)$ th epoch and propagated state estimation at k th epoch, respectively. Φ is the transition matrix and \mathbf{w}_k is the system noise matrix which follows the Gaussian distribution:

$$\mathbf{w}_k \sim \mathcal{N}(0, \mathbf{Q}) \quad (2).$$

where \mathbf{Q} is the covariance matrix of the system noise. The linearized measurement model is:

$$\mathbf{Z}_k = \mathbf{H} \mathbf{X}_k + \mathbf{v}_k \quad (3).$$

where \mathbf{Z}_k and \mathbf{H} are measurement vector and observation matrix, respectively. \mathbf{v}_k is the measurement noise matrix which follows the Gaussian distribution:

$$\mathbf{v}_k \sim \mathcal{N}(0, \mathbf{R}) \quad (4).$$

where \mathbf{R} is the covariance matrix of the measurement noise. The error covariance matrix in propagation is:

$$\mathbf{P}_{k/k-1} = \Phi \mathbf{P}_{k-1} \Phi^T + \mathbf{Q} \quad (5).$$

where $\mathbf{P}_{k/k-1}$ and \mathbf{P}_{k-1} are the predicted error covariance matrix at k th epoch and the updated error covariance matrix at $(k-1)$ th epoch, respectively. With the predicted error covariance matrix $\mathbf{P}_{k/k-1}$, observation matrix \mathbf{H} and the covariance matrix of the measurement noise \mathbf{R} , the Kalman gain can be calculated as:

$$\mathbf{K}_k = \mathbf{P}_{k/k-1} \mathbf{H}^T (\mathbf{H} \mathbf{P}_{k/k-1} \mathbf{H}^T + \mathbf{R})^{-1} \quad (6).$$

Finally, the state estimation vector and error covariance matrix with measurement update is:

$$\mathbf{X}_k = \mathbf{X}_k^- + \mathbf{K}_k (\mathbf{Z}_k - \mathbf{H} \mathbf{X}_k^-) \quad (7).$$

$$\mathbf{P}_k = (\mathbf{I} - \mathbf{K}_k \mathbf{H}) \mathbf{P}_{k/k-1} \quad (8).$$

For integrity monitoring of KF-based integration system shown in equation (7), the difficulty is that the current measurements cannot be mapped to the state estimation directly. In the other words, the updated state estimation is a balanced value between propagated state and the current measurements. The integrity risk can come from the propagated state which is related with the past epochs. The Kalman gain aggravates the problem further as it is a time-variant matrix. This form of KF recursive estimation violates the snapshot principle in autonomous integrity monitoring.

According to the above analysis, we try to establish a direct mapping function between the final state estimation and all kinds of input parameters, which can form a closed loop for integrity risk monitoring. Meanwhile the new measurement model under the mapping function should result in the same results equal to the KF recursive estimation. Inspired by the least square form proposed in [26], the mapping function can be rewritten as the new measurement model as follows:

$$\begin{bmatrix} \mathbf{Z}_k \\ \mathbf{X}_k^- \end{bmatrix} = \begin{bmatrix} \mathbf{H} \\ \mathbf{I} \end{bmatrix} \mathbf{X}_k + \begin{bmatrix} \mathbf{v}_k \\ \mathbf{v}_x \end{bmatrix} \quad (9).$$

where combine the measurement vector and propagated state vector as the new measurement vector. The new measurement model can be simplified as:

$$\mathbf{Y}_k = \mathbf{C} \mathbf{X}_k + \mathbf{v}_{zx} \quad (10).$$

where

$$\mathbf{Y}_k = \begin{bmatrix} \mathbf{Z}_k \\ \mathbf{X}_k^- \end{bmatrix}, \quad \mathbf{C} = \begin{bmatrix} \mathbf{H} \\ \mathbf{I} \end{bmatrix}, \quad \mathbf{v}_{zx} = \begin{bmatrix} \mathbf{v}_k \\ \mathbf{v}_x \end{bmatrix} \quad (11).$$

are the new measurement vector, new measurement observation matrix, and new observation noise vector, respectively. Meanwhile the noise vector is assumed to be zero mean Gaussian white noise and the corresponding covariance is:

$$\mathbf{v}_{zx} \sim \mathcal{N}(0, \mathbf{V}_k) \quad \mathbf{V}_k = \begin{bmatrix} \mathbf{R} & \mathbf{0} \\ \mathbf{0} & \mathbf{P}_{k/k-1} \end{bmatrix} \quad (12).$$

Using $\mathbf{W}=\mathbf{V}_k^{-1}$ as the weight value matrix, the weighted least square estimation can be written as:

$$\mathbf{X}_k = (\mathbf{C}^T \mathbf{W} \mathbf{C})^{-1} \mathbf{C}^T \mathbf{W} \mathbf{Y}_k \quad (13).$$

Then, we got the direct mapping function between state estimation and all input vectors which shows in ‘pseudo-snapshot’ form. However, it is not easy to conclude that the estimation \mathbf{X}_k is equal to the one calculated with classical EKF measurement update shown in equation (7) as the Kalman gain is not used in the above weighted least square estimation. The next subsection will derive the equivalence between each other.

B. Equivalence between Weighted Least Square and KF Recursive Estimation

Substitute equation (11) and equation (12) into equation (13), the estimation can be rewritten as:

$$\begin{aligned} \mathbf{X}_k &= \left(\begin{bmatrix} \mathbf{H}^T & \mathbf{I} \end{bmatrix} \begin{bmatrix} \mathbf{R}^{-1} & \mathbf{0} \\ \mathbf{0} & \mathbf{P}_{k/k-1}^{-1} \end{bmatrix} \begin{bmatrix} \mathbf{H} \\ \mathbf{I} \end{bmatrix} \right)^{-1} \begin{bmatrix} \mathbf{H}^T & \mathbf{I} \end{bmatrix} \begin{bmatrix} \mathbf{R}^{-1} & \mathbf{0} \\ \mathbf{0} & \mathbf{P}_{k/k-1}^{-1} \end{bmatrix} \begin{bmatrix} \mathbf{Z}_k \\ \mathbf{X}_k^- \end{bmatrix} \\ &= (\mathbf{H}^T \mathbf{R}^{-1} \mathbf{H} + \mathbf{P}_{k/k-1}^{-1})^{-1} \begin{bmatrix} \mathbf{H}^T \mathbf{R}^{-1} & \mathbf{P}_{k/k-1}^{-1} \end{bmatrix} \begin{bmatrix} \mathbf{Z}_k \\ \mathbf{X}_k^- \end{bmatrix} \end{aligned} \quad (14).$$

According to the matrix inversion lemma [30], the first part on the right side of equation (14) is equal to:

$$\begin{aligned} & (\mathbf{H}^T \mathbf{R}^{-1} \mathbf{H} + \mathbf{P}_{k/k-1}^{-1})^{-1} \\ &= \mathbf{P}_{k/k-1} - \mathbf{H}^T \mathbf{P}_{k/k-1} (\mathbf{H} \mathbf{P}_{k/k-1} \mathbf{H}^T + \mathbf{R})^{-1} \mathbf{H} \mathbf{P}_{k/k-1} \quad (15). \\ &= \mathbf{P}_{k/k-1} - \mathbf{K}_k \mathbf{H} \mathbf{P}_{k/k-1} \\ &= \mathbf{P}_k \end{aligned}$$

Then, equation (14) can be derived as:

$$\begin{aligned} \mathbf{X}_k &= \begin{bmatrix} \mathbf{H}^T \mathbf{R}^{-1} \mathbf{P}_k & \mathbf{P}_{k/k-1}^{-1} \mathbf{P}_k \end{bmatrix} \begin{bmatrix} \mathbf{Z}_k \\ \mathbf{X}_k^- \end{bmatrix} \\ &= \mathbf{P}_k \mathbf{H}^T \mathbf{R}^{-1} \mathbf{Z}_k + \mathbf{P}_k \mathbf{P}_{k/k-1}^{-1} \mathbf{X}_k^- \end{aligned} \quad (16).$$

According to equation (15), we can get another form of updated error covariance matrix as:

$$\mathbf{P}_k^{-1} = \mathbf{H}^T \mathbf{R}^{-1} \mathbf{H} + \mathbf{P}_{k/k-1}^{-1} \quad (17).$$

Substitute equation (17) to equation (6), the Kalman gain \mathbf{K}_k can be further expressed as:

$$\begin{aligned} \mathbf{K}_k &= \mathbf{P}_{k/k-1} \mathbf{H}^T (\mathbf{H} \mathbf{P}_{k/k-1} \mathbf{H}^T + \mathbf{R})^{-1} \\ &= (\mathbf{H}^T \mathbf{R} \mathbf{H} + \mathbf{P}_{k/k-1}^{-1})^{-1} \mathbf{H}^T \mathbf{R}^{-1} \\ &= \mathbf{P}_k \mathbf{H}^T \mathbf{R}^{-1} \end{aligned} \quad (18).$$

Substitute equation (17) and equation (18) to equation (16), we got the weighted least square state estimation as:

$$\begin{aligned} \mathbf{X}_k &= \mathbf{P}_k \mathbf{H}^T \mathbf{R}^{-1} \mathbf{Z}_k + \mathbf{P}_k \mathbf{P}_{k/k-1}^{-1} \mathbf{X}_k^- \\ &= \mathbf{K}_k \mathbf{Z}_k + \mathbf{P}_k (\mathbf{P}_k^{-1} - \mathbf{H}^T \mathbf{R}^{-1} \mathbf{H}) \mathbf{X}_k^- \\ &= \mathbf{X}_k^- + \mathbf{K}_k (\mathbf{Z}_k - \mathbf{H} \mathbf{X}_k^-) \end{aligned} \quad (19).$$

Finally, the equivalence between weighted least square and KF measurement update is proved encouragingly. The mapping

function established by the weighted least square form meets the snapshot principle. The next section, the integrity method based on solution separation is given in details with the weighted least square estimation.

III. INTEGRITY SOLUTION BASED ON KF-BASED SOLUTION SEPARATION

Solution separation method was firstly introduced to the GNSS integrity monitoring where the integrity risk was directly evaluated under the unified consideration of all single-element failure hypotheses and fault-free hypothesis [31,32]. The solution separation in positioning domain shows theoretical advantages over the classical least square residual-based method [33]. With a wide and mature application in RAIM, the solution separation method has been accepted as the baseline user algorithm in ARAIM, which is regarded as the next generation airborne RAIM solution [34]. The solution separation method is further expanded to Precise Point Positioning (PPP) integrity [35] and spoofing detection [36]. Based on the weighted least square form estimation in the above section, the KF-based solution separation algorithm is derived step by step in this section.

A. Integrity Risk Bounded by Solution Separation

In integrity monitoring, integrity risk P_{risk} is defined as the probability of providing a normal operation signal that is actually out of tolerance without warning the user in a given period of time. Here the maximum tolerable positioning error for an operation to safely proceed is called alert limit (AL). Correspondingly the protection level (PL) is a statistical error bound computed to guarantee the probability of error exceeding the bound is smaller than the defined integrity risk [37]. So, the integrity risk bounded by the protection level can be expressed as:

$$P\left(\left|\hat{\mathbf{X}} - \mathbf{X}\right| > AL \ \& \ PL < AL\right) \leq P_{risk} \quad (20).$$

where \mathbf{X} and $\hat{\mathbf{X}}$ are the actual position and estimated position, respectively.

For solution separation, its function in integrity risk can be regarded as the integrity risk allocation tree in integrity analysis [38,39]. The concept map of integrity risk allocation tree and the detailed implementation in solution separation is show in Fig. 2 and Fig. 3.

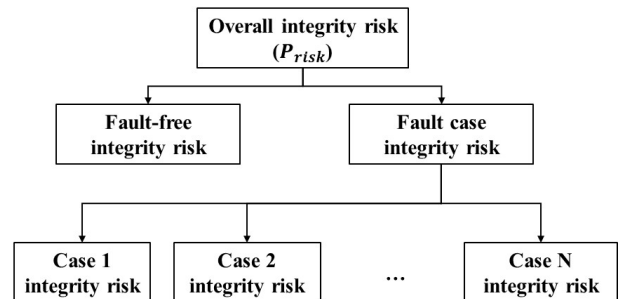


Fig. 2 Concept map of integrity risk allocation tree

As shown in Fig. 3, the operation of solution separation is to

i th fault hypothesis is:

$$P_{risk,H_i} = P\left\{\left(\left|\hat{\mathbf{X}}_i - \mathbf{X}\right| > AL \ \& \ PL < AL\right) \middle| H_i\right\} P(H_i) \quad (21).$$

where $P(H_i)$ represents the probability of i th fault hypothesis.

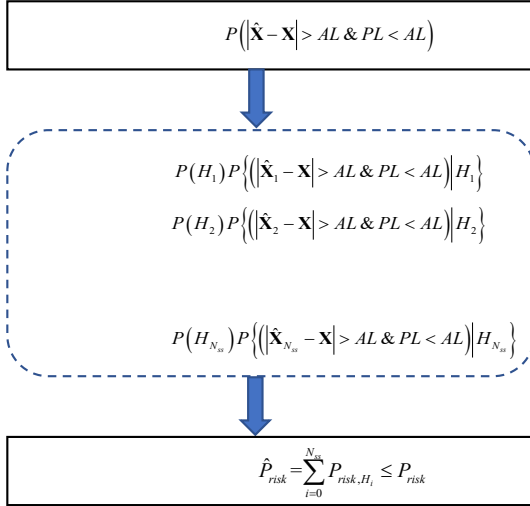


Fig. 3 Integrity Tree implementation in Solution Separation

Then, the integrity risk bounded by the solution separation can be written as follows:

$$\hat{P}_{risk} = \sum_{i=0}^{N_{ss}} P\left\{\left(\left|\hat{\mathbf{X}}_i - \mathbf{X}\right| > AL \ \& \ PL < AL\right) \middle| H_i\right\} P(H_i) \leq P_{risk} \quad (22).$$

where \hat{P}_{risk} is the estimated integrity risk bounded by the calculated protection level. It should be less than the defined integrity risk. N_{ss} represents the number of fault hypotheses. There are many researches on determining the number of fault hypotheses such as the maximum number of simultaneous faults proposed in the ARAIM baseline algorithm [40] and the feedback structure with probability accumulation proposed in [28]. Particularly the number of faulty sensors in one fault hypothesis is not limited to one.

B. Solution Separation with Sensor Exclusion

For solution separation operation, the weighted least square estimation derived in equation (13) is defined as the all-in-view solution under fault-free hypothesis. Regardless of the epoch k , the equation under fault-free hypothesis can be simplified and as:

$$\mathbf{X}^{(0)} = (\mathbf{C}^T \mathbf{W} \mathbf{C})^{-1} \mathbf{C}^T \mathbf{W} \mathbf{Y} \quad (23).$$

The fault-tolerance estimation $\mathbf{X}^{(i)}$ under the i th fault

hypothesis is calculated as:

$$\mathbf{X}^{(i)} = (\mathbf{C}^T \mathbf{W}^{(i)} \mathbf{C})^{-1} \mathbf{C}^T \mathbf{W}^{(i)} \mathbf{Y} \quad (24).$$

where $\mathbf{W}^{(i)}$ is the weighting matrix. The fault-tolerance estimation need to meet the following rule: Once the sensor is hypothesized as faulty under the i th fault hypothesis, all the weights in $\mathbf{W}^{(i)}$ corresponding to the measurements belonging to the faulty sensor should be set as zeros. Here the superscript (i) represents the i th fault hypothesis.

The fault detection is executed to test the fault hypotheses. As shown in Fig. 4, it is operated in positioning domain with the minimal detectable bias (MDB) $T_q^{(i)}$ as:

$$\left| \mathbf{X}_q^{(i)} - \mathbf{X}_q^{(0)} \right| \leq T_q^{(i)} \quad (25).$$

where the subscript q corresponds to the states related to the positioning components.

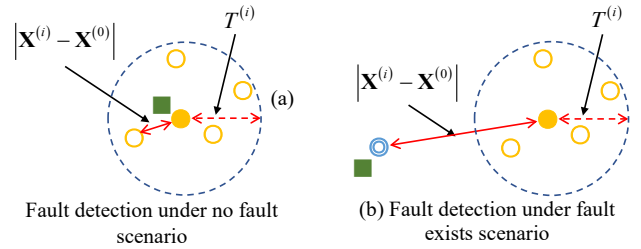


Fig. 4 Interpretation of fault detection in positioning domain. '■', '●', '○', '⊙' represent true position, fault-free positioning estimation, fault-tolerance positioning subset within faulty sensor and fault-tolerance positioning subset without fault sensor, respectively.

Then $T_q^{(i)}$ is also known as the threshold for fault detection of solution separation which is defined by [41]:

$$T_q^{(i)} = Q^{-1} \left(w_q \frac{P_{FA}}{N_{ss}} \right) \sigma_{ss,q}^{(i)} \quad (26).$$

where $\sigma_{ss,q}^{(i)}$ is extracted from the covariance matrix $\mathbf{P}_{ss}^{(i)}$ between the fault-free estimation and the estimation under the i th fault hypothesis.

$$\mathbf{P}_{ss}^{(i)} = \mathbf{U}^{(i)} \mathbf{V} \mathbf{U}^{(i)T} \quad (27).$$

$$\mathbf{U}^{(i)} = \left((\mathbf{C}^T \mathbf{W}^{(i)} \mathbf{C})^{-1} \mathbf{C}^T \mathbf{W}^{(i)} - (\mathbf{C}^T \mathbf{W} \mathbf{C})^{-1} \mathbf{C}^T \mathbf{W} \right) \quad (28).$$

where P_{FA} is the probability of false alert. w_q represents the weighted value allocated to this component. Q^{-1} is the inverse of the Q function, also known as the inverse of the tail probability of a zero mean unit normal distribution. The exclusion will be triggered once any of the tests fail. If all the tests pass, the protection level of solution separation is obtained by taking the maximum one across the $PL^{(i)}$,

$$PL^{(i)} = T^{(i)} + K_{md}^{(i)} \sigma^{(i)} \quad (29).$$

where $\sigma^{(i)}$ are the standard deviation the position solution $\mathbf{X}^{(i)}$

Considering the fault mode probability, the concept of integrity budget is chosen to determine the final PL [42]. The total integrity risk is identified as one budget and assigned to every fault mode. The integrity risk of corresponding fault mode equals to the product of the probability of fault mode and the probability of missed detection. As a form of integrity budget, equation (22) can be finally expressed as follows:

$$2P(H_0)Q(K_{md,0}) + \sum_{i=1}^{N_{ss}} P(H_i)Q(K_{md,i}) \leq P_{risk} \quad (30).$$

where the first item on the left side is the fault-free case and the factor is two because both tails of the error distribution need to be accounted for in solution separation. The second item is the sum of every fault hypothesis, weighted by the corresponding probability. To meet the integrity requirement, it is sufficient that the factors $K_{md}^{(i)}$ meet the integrity risk bounded by the estimation by fault-free hypothesis and all faulty hypotheses.

Substitute equation (29) to equation (30), the PL is determined by the following equation:

$$2P(H_0)Q\left(\frac{PL}{\sigma^{(0)}}\right) + \sum_{i=1}^{N_{ss}} P(H_i)Q\left(\frac{PL - T^{(i)}}{\sigma^{(i)}}\right) \leq P_{risk} \quad (31).$$

It is a complex process to solve the above equation exactly. It can be solved using a half-interval search in every component in most cases. The algorithm is summarized in detail in Algorithm 1.

Algorithm 1: Protection level calculation

Input: Integrity risk, P_{risk} ;

Tolerance for PL computation, TOL_{PL} ;

Number of fault hypotheses, N_{ss}

Every faulty hypothesis results, $P(H_i), \sigma^{(i)}, T^{(i)}$.

Fault-free hypothesis result, $P(H_0), \sigma^{(0)}$.

Output: Protection level (PL).

1. **for** fault hypothesis ($1 \leq i \leq N_{ss}$)

$$2. \quad PL_{low}^{(i)} = Q^{-1}\left(\frac{P_{risk}}{P(H_i)}\right)\sigma^{(i)} + T^{(i)}$$

$$3. \quad PL_{up}^{(i)} = Q^{-1}\left(\frac{P_{risk}}{P(H_i)(N_{ss} + 1)}\right)\sigma^{(i)} + T^{(i)}$$

4. **end for** every i

5. **for** fault-free hypothesis ($i = 0$)

$$6. \quad PL_{low}^{(0)} = Q^{-1}\left(\frac{P_{risk}}{2}\right)\sigma^{(0)}$$

$$7. \quad PL_{up}^{(0)} = Q^{-1}\left(\frac{P_{risk}}{2(N_{ss} + 1)}\right)\sigma^{(0)}$$

8. **end for** fault-free hypothesis

$$9. \quad PL_{low} = \max\{PL_{low}^{(0)}, PL_{low}^{(1)}, \dots, PL_{low}^{(N_{ss})}\}.$$

$$10. \quad PL_{up} = \max\{PL_{up}^{(0)}, PL_{up}^{(1)}, \dots, PL_{up}^{(N_{ss})}\}.$$

11. **while** $|PL_{up} - PL_{low}| > TOL_{PL}$

$$12. \quad PL_{half} = (PL_{up} + PL_{low})/2$$

$$13. \quad P_{risk, half} = 2P(H_0)Q\left(\frac{PL_{half}}{\sigma^{(0)}}\right) + \sum_{i=1}^{N_{ss}} P(H_i)Q\left(\frac{PL_{half} - T^{(i)}}{\sigma^{(i)}}\right)$$

14. **if** $P_{risk, half} > P_{risk}$

15. $PL_{low} = PL_{half}$

16. **else**

17. $PL_{up} = PL_{half}$

18. **end if**

19. **end while**

20. $PL = PL_{up}$

Finally, the detailed operation in KFSS processing is given in Fig. 5. The related core equations are also marked in the figure. As we have combined the measurement vector and propagated state vector as the new measurement vector, it is easy to detect whether it's observed sensor fault or propagated sensor fault with the fault-tolerance test of solution separation. Once one fault is detected, the fault exclusion is triggered immediately. The positioning results at this epoch need to be knocked down and calculated again to keep resilient and continuous navigation. In this step-by-step operation, to avoid the error divergence of recursive estimation, the corresponding matrices need to be reconstructed. If the excluded measurement is system state, the positioning estimation will be refined to the absolute least squared estimation of the measurements. It can be seen as a special circumstance of KFSS.

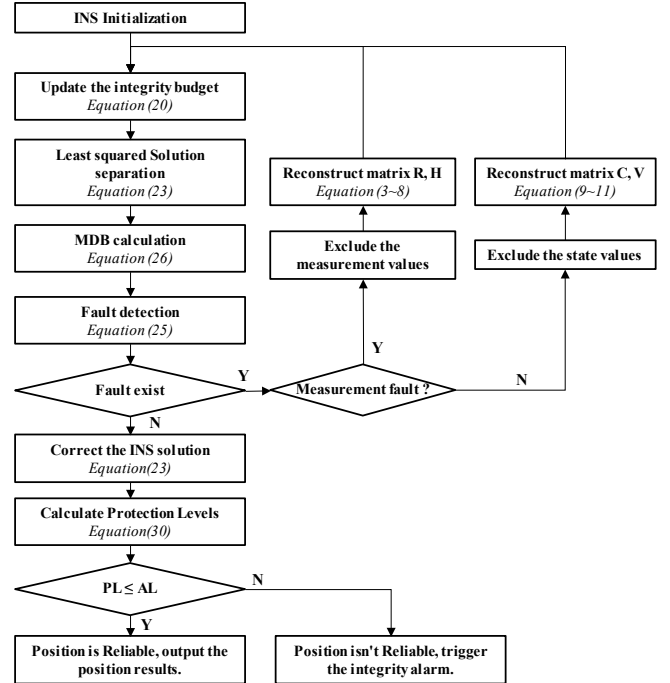


Fig. 5 Flow chart of the proposed integrity solution of Kalman filter based solution separation (KFSS).

The superiority of solution separation with sensor exclusion proposed in this paper includes two aspects: Firstly, we can analyze the impact of sensor fault on positioning result directly without considering the measurement relevance inside a single sensor. Secondly, for a multi-sensor integration system, the measurement exclusion is replaced by sensor exclusion, the number of fault hypothesis considered in equation (20) is substantially reduced. The disadvantage of computational

burden in solution separation is alleviated effectively [43,44].

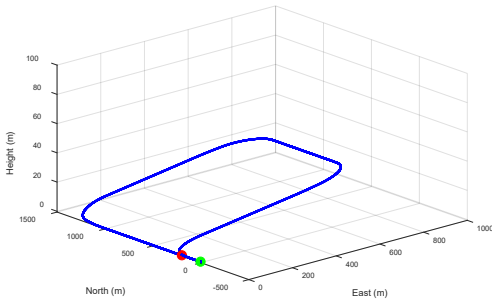
IV. SIMULATIONS, EXPERIMENTS AND DISCUSSION

To verify the feasibility of the proposed KFSS method for all source navigation integrity monitoring, simulations and experiments are given in this section. Considering the all-source navigation based on multi-sensor integration is really difficult to coordinate in actual experiment, the motivation of simulations is to match the all-source navigation scenario as much as possible, including sensor performance, signal faults and so on. Firstly, a tightly coupled INS/GNSS integration simulation and a loosely coupled INS/RTK/LiDAR/VINS multi-sensor integration simulation experiment are discussed in this section. Particularly, due to the independence of every satellite, the tightly coupled INS/GNSS model can be further expanded to tightly coupled multi-sensor integration in subsequent applications with independence of different sensors. Then, an experimental test based on a vehicle platform was conducted to evaluate the performance of the proposed KFSS method. INS, GNSS, LiDAR and camera are used for all-source navigation test. The details of implementation will be described in the following subsection. It should be noted that the above integration models are all developed based on the demos in reference [45], where the tightly couple and loosely couple are based on ‘Demo 7’ and ‘Demo 3’, respectively. It is accessible for method test and result verification as the book is opened to public and the demo codes are open sourced.

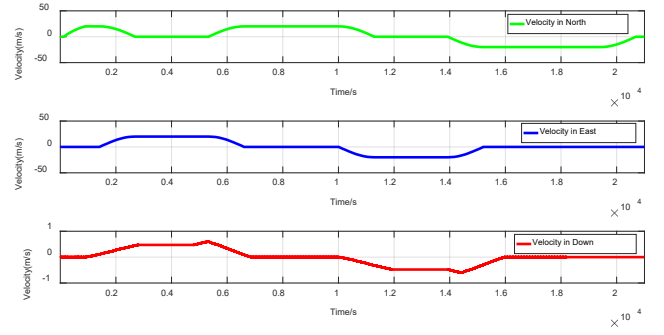
A. Scenario and Settings for simulation

A ground vehicle driving scenario is simulated and the trajectory is given in Fig. 6(a). The start position and final position are marked as green and red point, respectively. The corresponding velocity in North-East-Up (ENU) direction is given in Fig. 6(b). The whole period lasts 210 seconds. Both the tightly coupled integration and loosely coupled integration are tested based on this trajectory.

A consumer-grade inertial measurement unit (IMU) is chosen for integration. Some important simulation parameters such as gyro/accelerometer errors, GNSS pseudorange errors, and integrity settings are shown in Table I. The noises are random gaussian and the positioning outputs in every simulation are different from each other.



(a) Trajectory of 3D simulation



(b) Velocity of 3D motion

Fig. 6 Trajectory and velocity settings in the ground vehicle simulation experiment.

TABLE I
PARAMETERS SETTINGS USED IN SIMULATION

Subject	Parameter	Value	Application
INS errors	Gyro bias	200 deg/h	Section B/C
	Gyro random walk coefficient	1.000 deg/ \sqrt{h}	
	Accelerometer bias	9000 μg	
	Accelerometer random walk coefficient	1000 $\mu g\sqrt{Hz}$	
Observation sensor errors	Pseudorange measurement noise	2.5m	Section B
	Pseudorange rate measurement noise	0.1 m/s	
	positioning noise standard deviation of RTK	0.1m	Section C
	positioning noise standard deviation of LiDAR	0.3m	
positioning noise standard deviation of VINS	0.5m		
Integrity	Prior fault probability of INS	10^{-7}	Section B/C
	Prior fault probability of GNSS satellite	10^{-5}	Section B
	Prior fault probability of LiDAR and VINS	10^{-6}	Section C
	Integrity risk in vertical and horizontal components	9×10^{-8} / 1×10^{-8}	Section B/C

About the prior fault probability, the GNSS satellite probability introduced in ARAIM milestone report is accepted in this paper. GNSS constellation fault is not considered in this research [46]. Particularly, we believe the prior fault probability of INS is much less than that of GNSS satellites. 2 orders of magnitude are accepted in this simulation. For simplifying the computation, we assume the maximum simultaneous fault in the fault hypothesis is two. So take an example of one IMU and nine satellites, the number of fault hypotheses in KFSS and ARAIM is $N_{ss,KFSS}$ and $N_{ss,ARAIM}$, respectively. The results are as follows:

$$N_{ss,KFSS} = 1 + C_{10}^1 + C_{10}^2 = 56 \quad (32).$$

$$N_{ss,ARAIM} = 1 + C_9^1 + C_9^2 = 46 \quad (33).$$

It should be noted that the integrity algorithm for more than

one simultaneous fault in multi-sensor integration can be referred to the references mentioned in Section III. The final maximum simultaneous fault number should be determined by integrity budget and prior probability of every fault event.

B. Performance of Tightly INS/GNSS Coupled Integration

The integrity performance of KFSS method is compared with the baseline solution separation based RAIM, which is also well known as ARAIM.

The 17-state vector used in the model is:

$$\mathbf{X} = [\delta\boldsymbol{\varphi} \ \delta\mathbf{v} \ \delta\mathbf{p} \ \delta\mathbf{b}_a \ \delta\mathbf{b}_g \ \delta b_r \ \delta d_r] \quad (34).$$

where $\delta\boldsymbol{\varphi}$, $\delta\mathbf{v}$, and $\delta\mathbf{p}$ are the attitude, velocity and position error vector in three-dimensional frame, respectively. $\delta\mathbf{b}_a$ and $\delta\mathbf{b}_g$ are the accelerometer and gyroscope bias vector, respectively. δb_r and δd_r are the receiver clock bias and drift.

The system measurement vector can be expressed as

$$\mathbf{Z} = \begin{bmatrix} \rho^j \\ \dot{\rho}^j \end{bmatrix} \quad (35).$$

where ρ^j and $\dot{\rho}^j$ are the pseudo-range and pseudo-range rate of satellite j , respectively. It should be noted that it is the primary measurement vector of the Kalman filter. Then in the ‘pseudo-snapshot’ form of solution separation, the new measurement vector includes the system measurement vector \mathbf{Z} and state vector \mathbf{X} , simultaneously.

Fig. 7 shows the performance of tightly coupled INS/GNSS integration in positioning errors. Green, blue and red lines represent the outputs in north, east and up components, respectively. Table II gives the positioning performance statistics, including mean/max error, standard deviation (STD) and root mean square error (RMSE). The errors in northward and eastward positions are limited in 5 meters. Meanwhile the error in upward position is slightly larger which stays at 10 meters in most times. The RMSE in three directions are 0.87m, 2.53m and 16.20m. The integration period, also known as the update interval, is 1.0 second. Based on this tightly coupled INS/GNSS model, the fault detection ability and protection level performance are analyzed in the following parts.

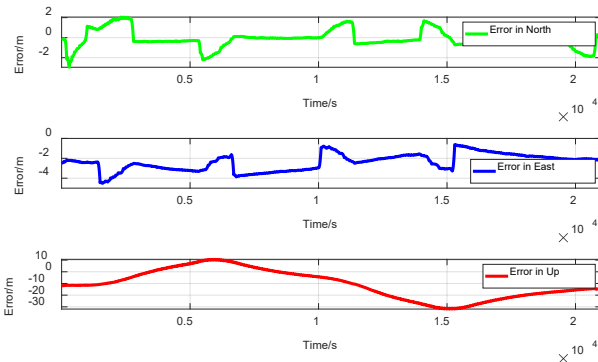


Fig. 7 Positioning errors of tightly coupled INS/GNSS integration implemented based on the open-sourced code [45].

TABLE II
POSITIONING PERFORMANCE OF TIGHTLY COUPLED INS/GNSS INTEGRATION

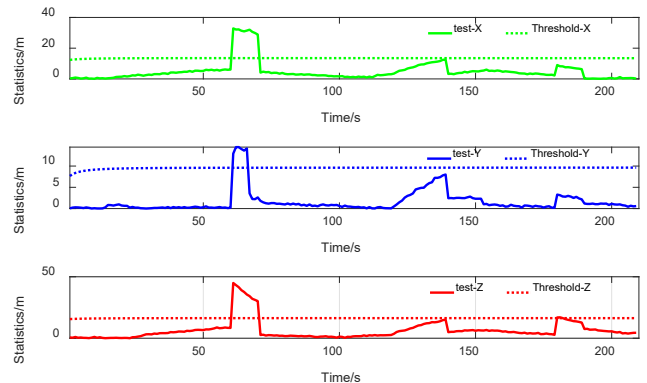
Item	North-axis	East-axis	Up-axis
Mean error	-0.14m	-2.40m	-10.69m
STD	0.86m	0.82m	12.17m
Max error	-2.95	-4.51m	-31.91
RMSE	0.87m	2.53m	16.20m

About the sensor fault, as shown in Table III, firstly two kinds of satellite observation faults were added in the processing. One is a slowly growing satellite pseudorange error (PRN-10 in this experiment) with 5 m/s between 120~140th epoch. The other one is two simultaneous satellites fault (PRN-14 and PRN 20 in this experiment) with a step error of 50 meters in pseudorange between 180~190th epoch. As mentioned above, the integrity risk from the propagation fault and the accumulation in recursive estimation is more difficult to detect and evaluate, compared to that from the measurement fault.

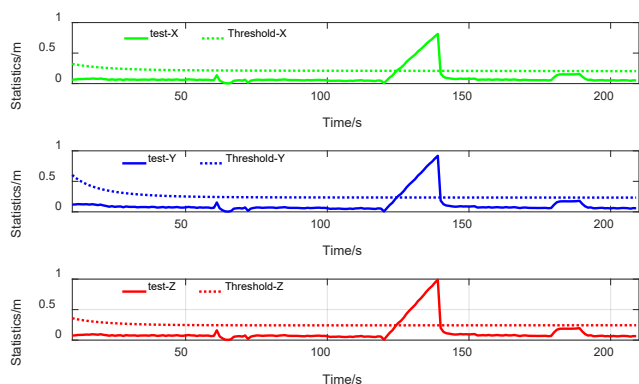
TABLE III
FAULT SETTING IN LOOSELY COUPLED MULTI-SENSOR INTEGRATION

No.	Fault event	Operation period/epoch	Fault description
1	INS fault	60~70	10*Special force
2	One satellite fault	120~140	5 m/s in PRN-10
3	Two satellites fault	180~190	50m in PRN-14 and PRN-20

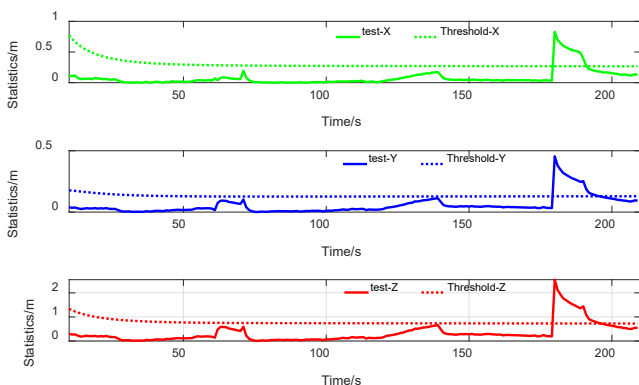
In this subsection, we also pay much attention to the propagation fault in KF estimation. A simple INS fault is simulated. Start from the 60th epoch, an accelerometer fault is taken place in the system and the fault lasts 10 epochs. As little literature defines the common concept of INS fault on integrity monitoring (e.g. type and amplitude), to help understand and implement this kind of fault, the accelerometer fault here is simulated as 10 times of the normal special force. We believe it can be accepted as the hazardous misleading information in the INS integrity evaluation. Then the test statistics for three fault-tolerance subsets and one regular case, are shown in Fig. 8. For calculation convenience, the fault detection ability is executed in earth centered earth fixed (ECEF) coordinate frame, which shown in X, Y, Z-axis in figures. It should be noted that the fault exclusion function is not added in this processing.



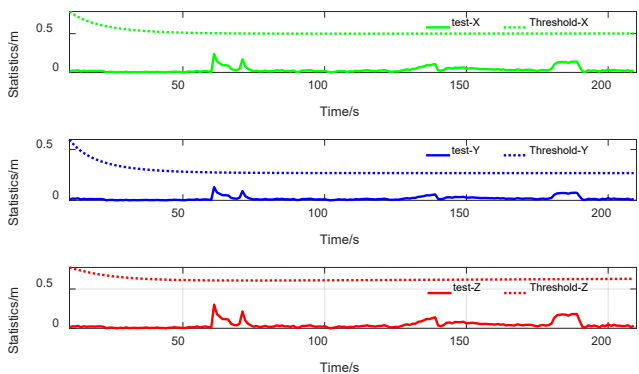
(a). Test statistics in INS-out subset



(b). Test statistics in faulty satellite-out subset



(c). Test statistics in two-faulty satellites-out subset



(d). Test statistics in a subset of excluding one normal satellite, namely a regular case

Fig. 8 Test statistics and thresholds in every subset of tightly coupled INS/GNSS integration. Lines from top to bottom in every subfigure are X, Y Z-axis, respectively. Solid lines and dotted lines are test statistics and thresholds, respectively.

Fig. 8(a) shows the test statistics and thresholds of INS-out subset in every epoch. Before the fault taken place, the test statistics are much less than the thresholds in all three axes. Then after the accelerometer fault is added in the 60th epoch, the test statistics exceed the thresholds in less than three epochs. The test statistics are affected more obvious due to the dynamic of vehicle. The KFSS method can detect the INS fault effectively and rapidly. The figure also shows that the test statistics of INS-out subset exceed the thresholds in some epochs when GNSS satellite fault took place. We'll discuss it later with the assist of normal solution subset.

The test statistics and thresholds of two satellite-out subsets related to faulty satellites in every epoch are shown in Fig. 8(b) and Fig. 8(c), where the former one is the slowly growing fault satellite subset and the latter one is the subset of two simultaneous faulty satellites. As shown in the figure, the slowly growing fault is difficult to be detected in time which resulted in slowly growing test statistics. However the KFSS method can detect this fault in less than four epochs. This detection time is very crucial for safety-critical navigation application as one parameter for integrity evaluation is time-to-alert.

The probability of two simultaneous faulty satellites is quite small. However with more and more GNSS constellations and satellites in orbit, the probability of this fault event cannot be ignored easily. As shown in Fig. 8(c), the step fault of two satellites fault is easy to be detected as the test statistics of next epoch after fault injection exceed the thresholds obviously. The impact of two satellites fault is much worse than that of one satellite fault. As shown in the figure, if the fault couldn't be excluded effectively, the output position would move to the faulty position quickly as the test statistics reduce obviously.

Furthermore, test statistics of one normal subset without any faults are shown in Fig. 8(d). Combined with the former three subfigures, the fact is that the INS fault and faulty satellite fault affected the other subsets simultaneously. It is easy to understand in solution separation that the impact of fault event will not only result in its corresponding fault-tolerance subset, but also affect the other subsets to some extent. However this impact is slightly different in the Kalman filter implementation. The impact of satellite fault to other subsets is similar to that of corresponding satellite-out subset. The test statistics grew with the slowly growing error and stepped with the step error. However on the other hand, during the period of INS fault, the impact has a decreasing trend. It's the unique phenomenon of recursive estimation as the temporal connectivity would aggravate the positioning error, which in turns hides the faulty propagation in the following epoch. It should be noted that there exists another peak after the INS fault finished in 70th epoch. That's because the special force returned to normal but the position in the last integration epoch was contaminated. That results that once faults are detected in Kalman filter, it should be excluded immediately and estimate the solution at this epoch again to avoid the fault propagation. Particularly if the fault comes from the propagation, the position initializations should be operated before the sensor is readmitted. That's also the reason that we refine to absolute least squared estimation in the case of state fault in Fig. 5.

Fig. 9 and Table IV give the positioning errors and RMSE in three scenarios: 1) no-fault setting; 2) faults exist without FDE function; 3) faults exist with KFSS FDE function. The errors are shown in blue, black and green lines, respectively. Particularly, the positioning errors during INS fault with FDE function is highlighted in pink dotted lines.

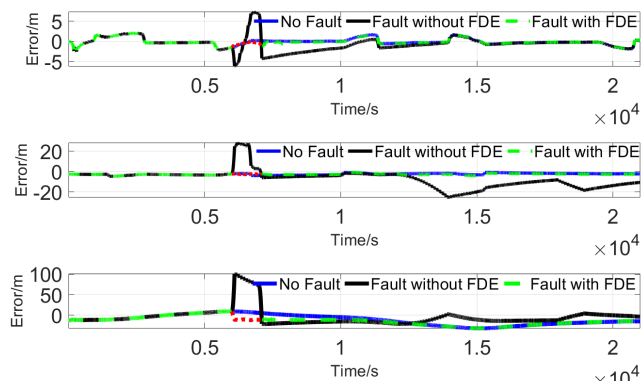


Fig. 9 Positioning errors under three scenarios in tightly coupled integration. From top to bottom are errors in X, Y and Z-axis, respectively.

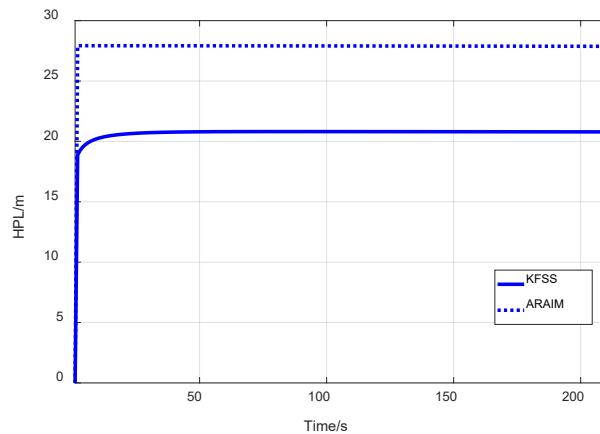
TABLE IV

POSITIONING PERFORMANCE UNDER THREE SCENARIOS IN TIGHTLY COUPLE

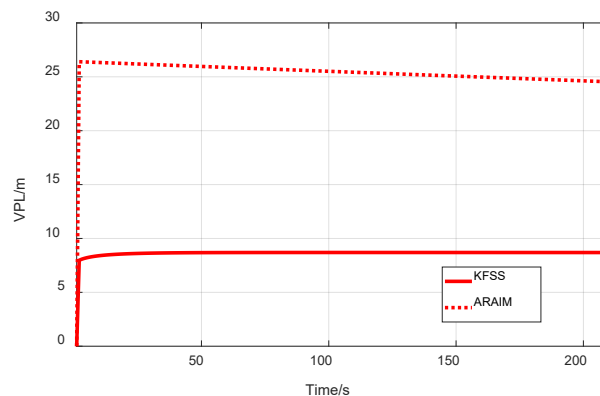
Item	No fault	Fault without FDE	Fault with FDE
RMSE in X-axis	0.86m	1.81m	0.86m
RMSE in Y-axis	2.56m	10.82m	2.70m
RMSE in Z-axis	16.17m	21.98m	17.29m

As shown in Fig. 9, errors increased with a different extent in all three axes without fault detection. Even the fault is finished, the system still needs a long time to recover, which is shown in black lines. On the contrary, the system with KFSS FDE function excluded the faulty sensors once the fault was detected. There's no obvious positioning accuracy loss during the whole process. Especially in INS fault period, the system immediately switched to GNSS-only mode after the fault was detected. Even though there was a slightly increase in positioning errors but the system can maintain normal work in short time and win valuable time for the control system to call for alternative solutions. The statistics in Table IV further verified the effectiveness of KFSS FDE function. The RMSE after FDE is similar to that of no-fault scenario.

Based on above tightly coupled model, the final protection levels between KFSS and ARAIM are compared. All the MDBs of fault-tolerance subsets are involved in the calculation. The horizontal protection level (HPL) and vertical protection level (VPL) results are shown in Fig. 10, respectively. The solid lines and dotted lines represent the outputs of KFSS and ARAIM, respectively.



(a). Horizontal protection levels



(b). Vertical protection levels

Fig. 10 Protection levels between KFSS and ARAIM

The results show that the HPL of KFSS keeps at 20 meters where that of ARAIM exceeds 27 meters. The advantage in vertical direction is much better. The VPL of KFSS is less than 10 meters compared with more than 31 meters of ARAIM. Compared to ARAIM, the proposed KFSS method monitored more fault hypotheses (56 vs 46) but got reduced protection levels both in horizontal and vertical directions effectively.

Compared to the classical ARAIM, the superiority of the proposed KFSS method on protection level computation can be discussed in three aspects. Firstly, the consistency of outputs of subsets are improved with Kalman filter, which results a smaller MDB for every subset. A smaller MDB directly contributes to the fault detection and protection level determination due to equation (25) and (28). Secondly, the advantage in vertical direction is much obvious compared to that of horizontal direction. That's because the introduction of INS information improved the vertical accuracy effectively. The thirdly and most importantly is that the INS fault is considered in the integrity risk, not only for positioning accuracy improvement. The price is that we need to detect and monitor more fault hypotheses. The integrity evaluation of KFSS is a closed loop respect to the integrity risk tree. The prior fault probability of INS is involved in the fault detection and protection level determination.

C. Performance of Loosely Coupled Multi-Sensor Integration

As little paper mentioned the integrity for loosely coupled integration. In this subsection the integrity for multi-sensor integration based on loosely couple is implemented and discussed. Four independent navigation systems are chosen in this model: INS, RTK, LiDAR and VINS. The INS maintains the consumer -grade IMU. The latter three systems can provide high accuracy three-dimensional positioning results. The multi-sensor navigation model is assumed for high accuracy application. Integrity for high accuracy navigation applications is also popular and urgent in current researches. Then the integration period is reduced to 0.5 second.

The 15-state vector used in the system model is:

$$\mathbf{X} = [\delta\boldsymbol{\phi} \quad \delta\mathbf{v} \quad \delta\mathbf{p} \quad \delta\mathbf{b}_a \quad \delta\mathbf{b}_g]^T \quad (36).$$

where $\delta\boldsymbol{\phi}$, $\delta\mathbf{v}$, and $\delta\mathbf{p}$ are the attitude, velocity and position error vector in three-dimensional frame, respectively. $\delta\mathbf{b}_a$ and $\delta\mathbf{b}_g$ are the accelerometer and gyroscope bias vector, respectively.

The 9-state primary measurement vector of Kalman filter can be expressed as

$$\mathbf{Z} = [\mathbf{p}_{RTK} \quad \Delta\mathbf{p}_{LiDAR} \quad \Delta\mathbf{p}_{VINS}]^T \quad (37).$$

where \mathbf{p}_{RTK} is the three-dimensional positioning outputs of RTK. $\Delta\mathbf{p}_{LiDAR}$ and $\Delta\mathbf{p}_{VINS}$ are the three-dimensional positioning changes of LiDAR and VINS, respectively. The measurement noise covariance matrix is set as:

$$\mathbf{R} = \begin{bmatrix} \boldsymbol{\sigma}_{RTK}^2 & 0 & 0 \\ 0 & \boldsymbol{\sigma}_{LiDAR}^2 & 0 \\ 0 & 0 & \boldsymbol{\sigma}_{VINS}^2 \end{bmatrix}^T \quad (38).$$

where $\boldsymbol{\sigma}_{RTK}$, $\boldsymbol{\sigma}_{LiDAR}$ and $\boldsymbol{\sigma}_{VINS}$ are the three-dimensional positioning noise standard deviations of RTK, LiDAR and VINS, respectively. Here the corresponding values are set as 0.1m, 0.3m, and 0.5m.

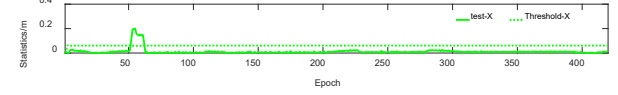
The fault setting is shown in Table V. Three faults took place during the processing. The INS fault is a step fault similar to the corresponding setting in tightly coupled integration. The fault of LiDAR and VINS are slowly growing errors.

TABLE V

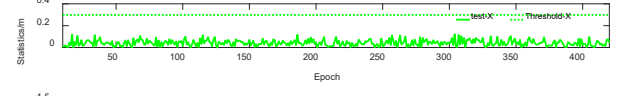
FAULT SETTING IN LOOSELY COUPLED MULTI-SENSOR INTEGRATION			
No.	Fault event	Operation period/epoch	Fault description
1	INS fault	50~60	10* special force
2	LiDAR fault	200~220	0.3 m/s in Y-axis
3	VINS fault	300~320	0.5 m/s in X-axis

The three-dimensional test statistics of every fault-tolerance subset are shown in Fig. 11. From (a) to (d) are subsets of INS-out, LiDAR-out, VINS-out and RTK-out, respectively. No fault exclusion function is added in this processing. Particular they are sensor-exclude subsets, which means all observable measurements related to the corresponding sensor will be excluded in the fault-tolerance estimation. For example, under the hypothesis of LiDAR fault, the three-dimensional

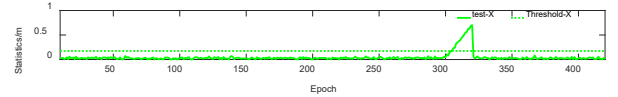
positioning results of LiDAR are simultaneously excluded to the subset positioning estimation.



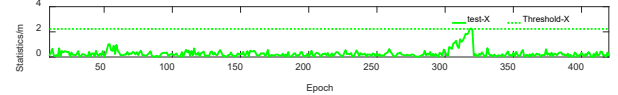
(a). Test statistics in INS-out subset



(b). Test statistics in LiDAR-out subset.



(c). Test statistics in VINS-out subset.



(d). Regular case: Test statistics in RTK-out subset.

Fig. 11 Test statistics and thresholds in every subset of loosely coupled INS/RTK/LiDAR/VINS integration. Lines from top to bottom in every subfigure are X, Y Z-axis, respectively. Solid lines and dotted lines are test statistics and thresholds, respectively.

It is encouraging to find that the KFSS method is still effective under the loosely coupled multi-sensor integration. As no matter that is sensor propagation or sensor measurement, the KFSS all involves it into fault-tolerance detection as one fault event. If the fault wasn't excluded immediately after detected, the normal subset (e.g. RTK-out subset in Fig. 11(d)) would be affected to some extent. The KFSS shows good performance

facing both step fault and slowly growing fault.

Finally, the positioning performance is shown in Fig. 12 and Table VI. The positioning errors were also divided into three scenarios: 1) no-fault setting; 2) faults exist without FDE function; 3) faults exist with KFSS FDE function, which shown in blue, black and red lines, respectively.

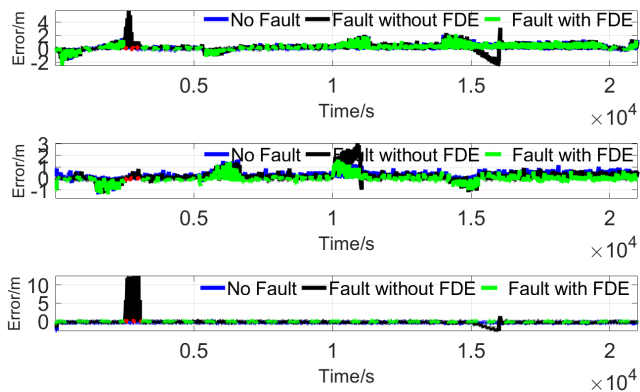


Fig. 12 Positioning errors under three scenarios in loosely coupled integration.

TABLE VI
POSITIONING PERFORMANCE UNDER THREE SCENARIOS IN LOOSELY COUPLE

Item	No fault	Fault without FDE	Fault with FDE
RMSE in X-axis	0.44m	0.59m	0.45m
RMSE in Y-axis	0.37m	0.45m	0.30m
RMSE in Z-axis	0.40m	1.06	0.19m

The figure shows that the impact of sensor fault can be up to meters, which is fatal and unacceptable in high accuracy navigation. Relatively, the positioning with KFSS FDE can reduce the accuracy loss to the minimum. Particular, as the LiDAR and VINS observations are excluded under faulty periods, the positioning accuracy is improved due to the performance of RTK. The RMSE under the third scenario is less than that under no-fault scenario in Y-axis and Z-axis.

About the output protection levels, as shown in Fig. 13, the horizontal protection level is nearly 4 meters and the vertical one maintains at about 2.5 meters. The protection levels can bound the positioning error appropriately and tightly.

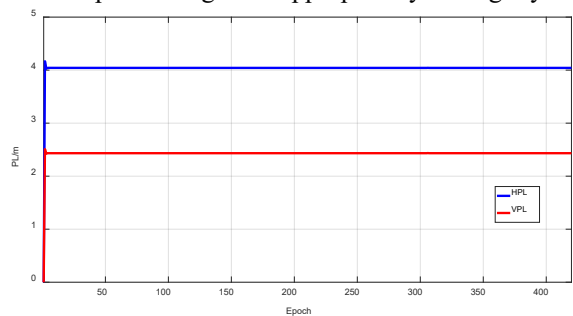


Fig. 13 Protection levels calculation in loosely coupled multi-sensor integration

D. Performance of All-source Navigation Experiment

The vehicle platform for all-source navigation experiment is established by the Intelligent Positioning and Navigation Laboratory (IPN), Hong Kong Polytechnic University. All the

localization-based related sensors are equipped in a compact sensor kit on the top of the vehicle, which is shown in Fig. 14. The details of the sensor description are as follows:

- IMU: Xsens Mti10, 100Hz;
- GNSS: Ublox M8T, GPS/BDS, 1Hz;
- LiDAR: Velodyne HDL 32E, 360 Horizontal Field of View (FOV), -30+10 vertical FOV, 80 meters in range, 10Hz;
- Camera: Grasshopper3 5.0 MP (GS3-U3-51S5C-C), fisheye lens Fujinon FE185C057HA-1, 185 HFOV, 185 V-FOV, 10Hz;

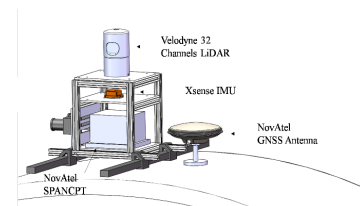
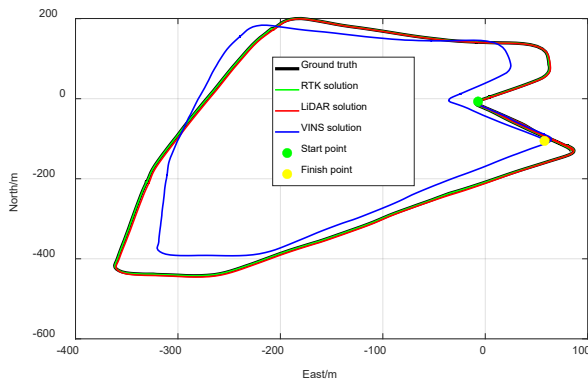


Fig. 14 Vehicle platform for sensor data collection

The actual kinematic automobile signal was collected in East Tsim Sha Tsui, Hong Kong. It's a representative urban canyon place that easy to result in faulty measurement due to model mismatch and sensor misspecification. We choose this challenging environment to test the feasibility of proposed KFSS method. The ground truth used in this experiment is provided by Novatel SPAN-CPT, a GNSS-IMU (fiber optics gyroscope) navigation system. The device is widely used for accurate localization assignments on mobile platforms. For laser odometry, the point registration algorithm Normal Distribution Transformation (NDT) is accepted for positioning solution in this experiment [47]. For visual odometer estimation, the open-sourced VINS-MONO algorithm, which tightly couples visual odometry with IMU estimation to output an optimized localization result is adopted in this experiment [48]. As it is a high accuracy application, the received GNSS signal of Ublox receiver is corrected from the RTK signal sent from local public base stations. The ground truth trajectory and single sensor solution of RTK, LiDAR and VINS are shown in Fig. 15.



(a). Kinematic trajectory in Google Earth

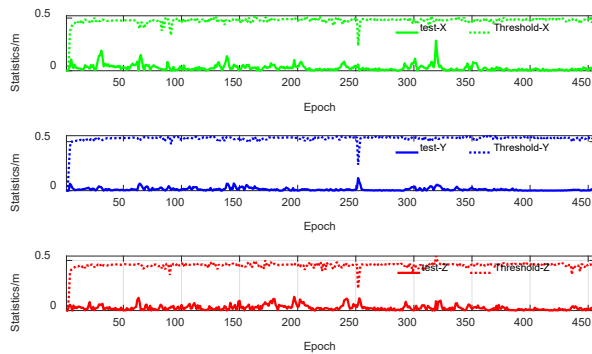


(b). Ground truth and single sensor position solution.

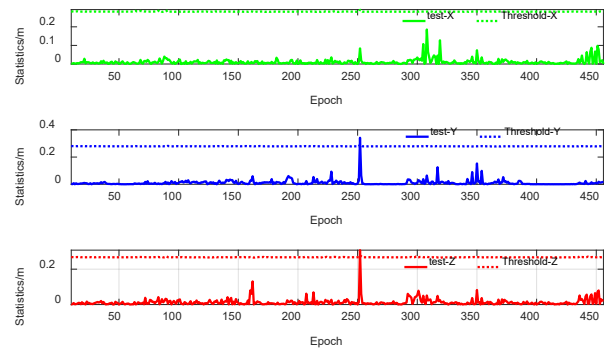
Fig. 15 Ground truth and single sensor position solution of GNSS RTK, LiDAR and VINS. It is shown in 2-dimensional horizontal components of ENU coordinate system.

About the signal sensor performance, it can be seen that the accuracy of RTK is the best. The error compared to ground truth can be as small as centimeter level. The accuracy of LiDAR in most cases is less than one meter but sometimes the accumulative error can exceed one meter. The accuracy of camera is the worst of the three. The accumulative error can be as large as about meters. That also supports the algorithm that we choose positioning changes of LiDAR and VINS in the observable vector of Kalman filter. The three-dimensional positioning noise standard deviations of RTK, LiDAR and VINS are set as 0.1m, 0.3m, and 0.5m, respectively.

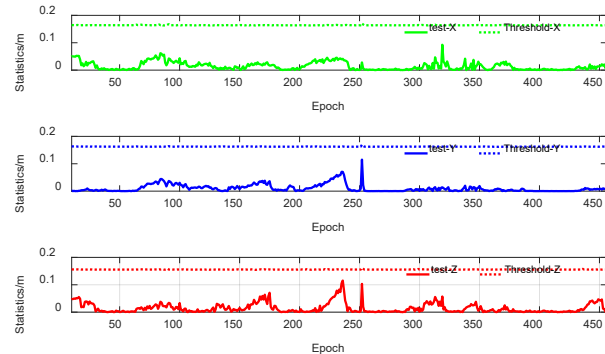
As four sensors are involved in this experiment, we only monitor one fault hypothesis. That's because once two simultaneous faults happen, it is difficult to exclude the faulty sensors as redundant measurements are lack. The three-dimensional test statistics of every fault-tolerance subset are shown in Fig. 16. From (a) to (d) are subsets of INS-out, LiDAR-out, VINS-out and RTK-out, respectively.



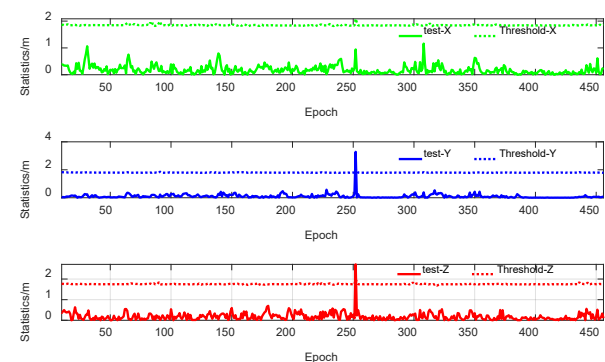
(a). Test statistics in INS-out subset



(b). Test statistics in LiDAR-out subset.



(c). Test statistics in VINS-out subset.



(d). Test statistics in RTK-out subset.

Fig. 16 Test statistics and thresholds in every subset of vehicle experiment. Lines from top to bottom in every subfigure are X, Y Z-axis, respectively. Solid lines and dotted lines are test statistics and thresholds, respectively.

As shown in the figure, in most cases all sensor-exclude subsets resulted in regular circumstances. The navigation is available in the above corresponding period. The KFSS method is effective during the actual kinematic experiment. But at the 251st epoch, both the LiDAR-out subset and RTK-out subset detected fault. That's means at least two sensors are faulty at this epoch. As mentioned above, we only have four sensors. It can not exclude the faulty measurements easily, particularly once the two faulty sensors resulted in the same hazardous positioning result. This experiment revealed the inherent limitation on fault exclusion. Redundant information is necessary for integrity monitoring. Some related works mentioned to depend on sensors with high priority such as INS at this challenging circumstance. That's beyond the scope of this paper. We chose to trigger the integrity alert in this

experiment and the navigation output is not reliable at this epoch.

After excluding the unavailable epoch, the positioning performance of loosely coupled INS/RTK/LiDAR/VINS integration is shown in Fig. 17 and Table VII. The calculated HPL and VPL is shown in Fig. 18.

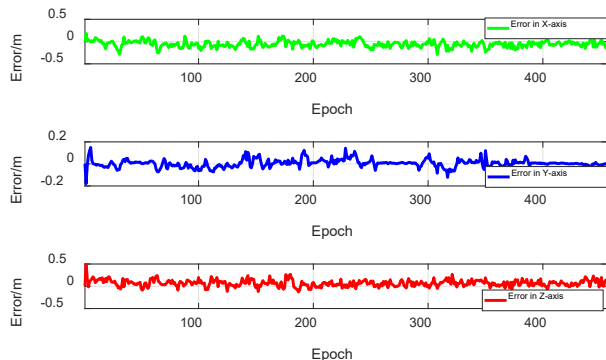


Fig. 17 Positioning errors of navigation integration in vehicle experiment. It is shown in ECEF coordinate frame

TABLE VII
POSITIONING PERFORMANCE OF NAVIGATION SYSTEM

Item	X-axis	Y-axis	Z-axis
Mean error	-0.06m	0.01m	0.07m
STD	0.07m	0.04m	0.07m
Max error	0.19m	0.15m	0.50m
RMSE	0.09m	0.04m	0.10m

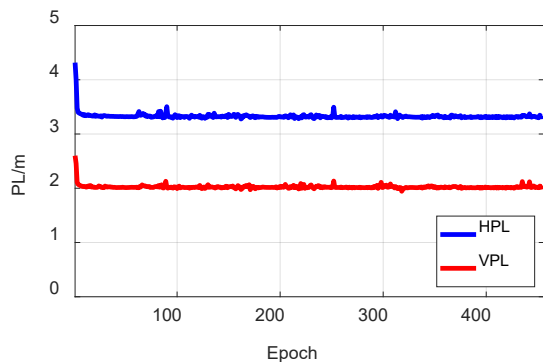


Fig. 18 Protection levels calculation in vehicle experiment

As shown in the figure and table, the positioning error on each axis is less than 0.5m in the whole experiment and below 0.2 m in most cases, which shows a high accuracy performance. The RMSE doesn't exceed 0.10m in every direction. About the protection levels, the HPL is less than 3.5m and the VPL is about 2.0m in most cases. Considering that the system model is still based on a consumer -grade IMU, it can be estimated aggressively that the protection levels can be significantly reduced enhanced by a higher grade IMU. This conclusion is encouraging to high accuracy safety-critical navigation applications such as autonomous driving as their safe space is very limited.

V. DISCUSSIONS

A. Performance and Limitation of Standard Kalman Filter

It should be noted that the proposed KFSS method is implemented on standard form of extended Kalman filter in this paper. It has to be considered that the performance of Kalman filter may not be acceptable in some time-varying and uncertain operation conditions due to its limitations in linearity and statistical assumptions. However as our method didn't touch or modify the fusion process inside Kalman filter, it can be further extended to other KF methods to improve its limitations in linearity and statistical assumptions. For example, sigma-point KF (SPKF) is a better choice for nonlinear systems [49, 50]. SPKF can captures the posterior mean and covariance accurately to the 2nd order (Taylor series expansion) for any nonlinearity (3rd order accuracy is achieved if the prior random variable has a symmetric distribution), which provides superior performance over the current KF and EKF by better accounting for nonlinearities and accommodating asynchronous and lagged sensor measurements. The statistic assumptions and error modelling are another problem that limit the classical KF application in uncertain operation conditions. One feasible method is to update the process noise covariance and measurement noise covariance online to improve the stability and sensitivity performance of system [51]. Another method is to collect experimental data as much as possible or do exhausted/greedy simulations to verify the good of fit between sensor signals and system models [25,52].

B. Integrity Requirements for Specific Application

The focus of this paper is to propose one user algorithm for integrity monitoring of multi-sensor navigation system. As integrity is the measure of trust for specific safety-critical applications, several parameters such as ALs and integrity risk, need to be determined by corresponding requirements to define safe space and avoid hazardous situations. For example, the horizontal AL for civil airplane during en-route operation can be as large as several nautical miles but that for autonomous driving need to be narrowed to meters. The decomposition of AL also needs to serve for the corresponding requirement. We break down the AL to horizontal and vertical components for civil airplane in most cases, but for grounding vehicle, we care more about the lateral and longitudinal directions [53]. It is crucial to define and quantify the hazardous misleading information (HMI) for the specific application. The integrity risk, also known as the probability of hazardous misleading information (PHMI), is the essential input requirement to calculate the PL. The comparison of ALs and PLs will directly determine the availability of system at this epoch. The standard deviation and prior probability of fault for different sensors are parameters for solution separation. As a successful application of solution separation, the baseline ARAIM user algorithm define them in integrity support message (ISM) [40]. It can be used for reference to improve the proposed method in this paper. Particularly learning from the monitor of GNSS signal-in-space, it needs to characterize the errors in light of known or predictable characteristics and ensure that these parameters will

continue to bound or overbound the future fault-free situations [54]. It is necessary to estimate and determine the standard deviation and prior probability of fault based on observation data and comprehensive simulations for specific application.

VI. CONCLUSION

Based on the integrity application in multi-sensor navigation integration, a new Kalman filter based solution separation (KFSS) method is proposed in this paper. For the KFSS processing, the classical EKF estimation is remodeled as the weighted least square form in preparation for the following integrity evaluation. The propagation states are involved in the new measurement vector to keep the integrity risk produced by both the temporal connectivity and system propagation is considered in the integrity monitoring effectively. Then, the fault detection and exclusion are operated in positioning domain based on solution separation. Particularly, the solution separation is enhanced by sensor exclusion, which is pretty applicable for all-source navigation. Furthermore, the protection levels in horizontal and vertical dimensions are determined with the concept of integrity budget. The proposed method gets the rid of limitations on sensor types, number of simultaneous faults and integration models.

The open sourced tightly coupled INS/GNSS integration and loosely coupled INS/RTK/LiDAR/VINS multi-sensor integration are simulated and discussed with different types of faults. The KFSS method can detect both the propagation fault and measurement fault. The fault exclusion operation with refined matrix reconstruction can maintain the positioning accuracy to overcome the error divergence caused by the state fault propagation. Furthermore, an actual vehicle kinematic experiment with multi-sensor navigation system is implemented to verify the feasibility of KFSS for all-source navigation. The effectiveness and superiority of KFSS are verified under autonomous driving scenario. The experiment also reveals the limitation of dependence on redundant measurements. The protection levels calculated with actual signal also shows potential superiority in lane level applications. Compared to the ARAIM method, the horizontal and vertical protection level outputs can be reduced greatly. It is a positive signal to keep the availability of navigation system in complex and challenging circumstances. The proposed KFSS method is applicable for the performance evaluation of the plug and play all-source navigation, especially the navigation requirements of safety-critical applications such as autonomous driving and unmanned aerial vehicles.

The future work includes two aspect: The authors are now working on multi-sensor dynamic vehicle prototype platform construction and build the all-source navigation scenario as far as possible. It will verify the feasibility of the KFSS solution under different scenarios in the near future. Then, the impact of different levels of IMU for PL reduction in autonomous driving application is another focus.

ACKNOWLEDGMENT

The simulation platform is developed based on the open source demo provided by Dr. Paul Groves, University College London, UK. Thanks for his outstanding work.

REFERENCES

- [1] J. McNeff, "Changing the Game Changer—The Way Ahead for Military PNT," *Inside GNSS*, vol.5, no.8, pp. 44-51, Dec. 2010.
- [2] P. Groves, "Assured PNT Through Multiple Diverse Technologies," In *Proc. of ION GNSS+ 2016*, Portland, Oregon, USA, Sept. 2016, pp. 946-958.
- [3] Y. X. Yang, "Resilient PNT Concept Frame," *Acta Geodaetica et Cartographica Sinica*, vol. 47, no. 7, pp. 893-898, 2018.
- [4] L. Hsu, Y. Gu, Y. Huang and S. Kamijo, "Urban Pedestrian Navigation Using Smartphone-Based Dead Reckoning and 3-D Map-Aided GNSS," *IEEE Sensors Journal*, vol. 16, no. 5, pp. 1281-1293, Mar. 2016.
- [5] T. Song, N. Capurso, X. Cheng, *et al.*, "Enhancing GPS with lane-level navigation to facilitate highway driving," *IEEE Transactions on Vehicular Technology*, vol. 66, no. 6, pp. 4579-4591, June 2017.
- [6] S. Zahran, A. M. Moussa, A. B. Sesay and N. El-Sheimy, "A New Velocity Meter Based on Hall Effect Sensors for UAV Indoor Navigation," *IEEE Sensors Journal*, vol. 19, no. 8, pp. 3067-3076, Apr. 2019.
- [7] A. Jolfaei and K. Kant, "On the Silent Perturbation of State Estimation in Smart Grid," *IEEE Transactions on Industry Applications*, vol. 56, no. 4, pp. 4405-4414, July-Aug. 2020.
- [8] Y. Lee, B. Bian, "Advanced RAIM Performance Sensitivity to Deviations in ISM Parameter Values," In *Proc. of ION GNSS+ 2017*, Portland, Oregon, USA, Sept. 25-29, 2017, pp. 2338-2358.
- [9] T. Walter, P. Enge, J. Blanch, B. Pervan, "Worldwide vertical guidance of aircraft based on modernized GPS and new integrity augmentations," *Proceedings of the IEEE*, vol. 96, no. 12, pp. 1918-1935, Dec. 2008.
- [10] T. Walter, P. Enge, "Weighted RAIM for precision approach," *PROCEEDINGS OF ION GPS*, vol. 8, no. 1, pp. 1995-2004, Sep. 1995.
- [11] Q. Meng, J. Liu, Q. Zeng, *et al.*, "Impact of one satellite outage on ARAIM depleted constellation configurations," *Chinese Journal of Aeronautics*, vol.32, no. 4, pp. 967-977, Apr. 2019.
- [12] W. Wen, X. Bai, Y.C. Kan, L.T. Hsu, "Tightly Coupled GNSS/INS Integration via Factor Graph and Aided by Fish-Eye Camera," *IEEE Transactions on Vehicular Technology*, vol. 68, no. 11, pp. 10651-10662, Sep. 2019.
- [13] W. Jiang, D. Liu, B. Cai, *et al.*, "A Fault-Tolerant Tightly-Coupled GNSS/INS/OVS Integration Vehicle Navigation System Based on a FDP Algorithm," *IEEE Transactions on Vehicular Technology*, vol. 68, no. 7, pp. 6365-6378, July, 2019.
- [14] H. Rong, C. Peng, Y. Chen, L. Zou, Y. Zhu and J. Lv, "Adaptive-Gain Regulation of Extended Kalman Filter for Use in Inertial and Magnetic Units Based on Hidden Markov Model," *IEEE Sensors Journal*, vol. 18, no. 7, pp. 3016-3027, Apr. 2018.
- [15] B. Cui, X. Wei, X. Chen, *et al.*, "On Sigma-Point Update of Cubature Kalman Filter for GNSS/INS Under GNSS-Challenged Environment," *IEEE Transactions on Vehicular Technology*, vol. 68, no. 9, pp. 8671-8682, Jul. 2019.
- [16] Y. Zhao, "Cubature + Extended Hybrid Kalman Filtering Method and Its Application in PPP/IMU Tightly Coupled Navigation Systems," *IEEE Sensors Journal*, vol. 15, no. 12, pp. 6973-6985, Dec. 2015.
- [17] Q. Zhang, L. Zhao, L. Zhao and J. Zhou, "An Improved Robust Adaptive Kalman Filter for GNSS Precise Point Positioning," *IEEE Sensors Journal*, vol. 18, no. 10, pp. 4176-4186, May 2018.
- [18] R. S. Young, G. A. McGraw, "Fault detection and exclusion using normalized solution separation and residual monitoring methods," *Navigation*, vol. 50, no. 3, pp. 151-169, Sep. 2003.
- [19] M. Joerger, B. Pervan, "Kalman filter-based integrity monitoring against sensor faults," *Journal of Guidance, Control, and Dynamics*, vol. 36, no. 2, pp. 349-361, Feb. 2013.
- [20] J. D. Jurado, J. F. Raquet, "Autonomous and Resilient Management of All-Source Sensors," In *Proceedings of the ION 2019 Pacific PNT Meeting*, Honolulu, Hawaii, USA, April 2019, pp. 142-159.
- [21] G. D. Arana, M. Joerger, M. Spenko, "Efficient integrity monitoring for kf-based localization," In *Proc. ICRA 2019*, Montreal, QC, Canada, May 20-24, 2019, pp. 6374-6380.
- [22] W. Pan, X. Zhan, X. Zhang, "Fault exclusion method for ARAIM based on tight GNSS/INS integration to achieve CAT-I approach," *IET Radar*,

- Sonar & Navigation*, vol. 13, no. 11, pp. 1909-1917, Jun. 2019.
- [23] S. Bhattacharyya, D. Gebre-Egziabher, "Kalman filter-based RAIM for GNSS receivers," *IEEE Transactions on Aerospace and Electronic Systems*, vol. 51, no. 3, pp. 2444-2459, Sep. 2015.
- [24] S. Sukkarieh, E. M. Nebot, H. F. Durrant-Whyte, "A high integrity IMU/GPS navigation loop for autonomous land vehicle applications," *IEEE Transactions on Robotics and Automation*, vol. 15, no. 3, pp. 572-578, Jun. 1999
- [25] L. Hsu, H. Tokura, N. Kubo, Y. Gu and S. Kamijo, "Multiple Faulty GNSS Measurement Exclusion Based on Consistency Check in Urban Canyons," *IEEE Sensors Journal*, vol. 17, no. 6, pp. 1909-1917, Mar. 2017.
- [26] Hewitson, J. Wang, "Extended receiver autonomous integrity monitoring (E RAIM) for gnss/ins integration," *Journal of Surveying Engineering*, vol. 136, no. 1, pp. 13-22, Jan. 2010.
- [27] A. Lay-Ekuakille, A. Trotta and G. Vendramin, "Beamforming-Based Acoustic Imaging for Distance Retrieval," In *Proceedings of 2008 IEEE Instrumentation and Measurement Technology Conference*, Victoria, BC, USA, June, 2008, pp. 1466-1470.
- [28] Q. Meng, J. Liu, Q. Zeng, *et al.*, "Improved ARAIM fault modes determination scheme based on feedback structure with probability accumulation," *GPS Solutions*. vol. 23, no. 1, pp. 16, Jan. 2019
- [29] B. Yang, L. Guo, F. Li, J. Ye and W. Song, "Vulnerability Assessments of Electric Drive Systems Due to Sensor Data Integrity Attacks," *IEEE Transactions on Industrial Informatics*, vol. 16, no. 5, pp. 3301-3310, May 2020.
- [30] D. J. Tylavsky, G. R. Sohie, "Generalization of the matrix inversion lemma," *Proceedings of the IEEE*, vol. 74, no. 7, pp. 1050-1052, Jul. 1986.
- [31] B. S. Pervan, S. P. Pullen, J. R. Christie, "A multiple hypothesis approach to satellite navigation integrity," *Navigation*, vol. 45, no. 1, pp. 61-71, Mar. 1998.
- [32] T. Walter, J. Blanch, P. Enge, "Reduced subset analysis for multi-constellation ARAIM," In *Proceedings of ION ITM 2014*, San Diego, California, USA. Jan 2014, pp. 89-98.
- [33] M. Joerger, F. C. Chan, B. Pervan, "Solution Separation Versus Residual-Based RAIM," *NAVIGATION: Journal of the Institute of Navigation*, vol. 61, no. 4, pp. 273-291, Dec. 2014
- [34] EU-US Cooperation on Satellite Navigation Working Group C, "ARAIM Technical Subgroup Milestone 3," February 25, 2016. [Online] Available: <https://www.gps.gov/policy/cooperation/europe/2016/working-group-c/>.
- [35] K. Gunning, J. Blanch, T. Walter, *et al.*, "Design and Evaluation of Integrity Algorithms for PPP in Kinematic Applications," In *Proceedings of ION GNSS+ 2018*, Miami, Florida, USA, Sep 2018, pp. 1910-1939.
- [36] H. Kuusniemi, J. Blanch, Y. H. Chen, S. Lo, P. Enge, "Feasibility of Fault Exclusion Related to Advanced RAIM for GNSS Spoofing Detection". In *Proceedings of ION GNSS+ 2017*, Portland, Oregon, USA, Sep. 25-29, 2017, pp. 2359-2370.
- [37] N. Zhu, J. Marais, D. Bétaille, M. Berbineau, "GNSS position integrity in urban environments: A review of literature," *IEEE Transactions on Intelligent Transportation Systems*, vol. 19, no. 9, pp. 2762-2778, Jan. 2018.
- [38] S. Pullen, T. Walter, P. Enge, "Integrity for non-aviation users," *GPS World*, vol. 22, no.7, pp. 28-36, Jul. 2011.
- [39] I. Martini, M. Rippl, M. Meurer, "Integrity Support Message Architecture Design for Advanced Receiver Autonomous Integrity Monitoring," In *Proceedings of European Navigation Conference*, Vienna, Austria, Apr. 23, 2013, pp. 23-25.
- [40] J. Blanch, T. Walter, P. Enge, *et al.*, "Baseline advanced RAIM user algorithm and possible improvements," *IEEE Transactions on Aerospace and Electronic Systems*, vol.51, no. 1, pp. 713-732, Apr. 2015
- [41] EU-US Cooperation on Satellite Navigation Working Group C, "ARAIM Technical Subgroup Milestone 2," February 11, 2015. [Online] Available: <https://www.gps.gov/policy/cooperation/europe/2015/working-group-c/>.
- [42] J. Blanch, T. Walter, and P. Enge, "RAIM with optimal integrity and continuity allocations under multiple failures," *IEEE Transactions on Aerospace and Electronic Systems*, vol. 46, no. 3, pp. 1235-1247, Aug. 2010
- [43] Y. Ge, Z. Wang, Y. Zhu, "Reduced ARAIM monitoring subset method based on satellites in different orbital planes," *GPS Solutions*, vol. 21, no. 4, pp. 1443-1456, Oct. 2017.
- [44] Q. Meng, J. Liu, Q. Zeng, *et al.*, "Reduced ARAIM Subsets method determined by Threshold for Integrity Risk," In *Proceedings of CSNC 2018*, Harbin, China, May. 2018, pp. 701-711.
- [45] P. D. Groves, *Principles of GNSS, inertial, and multisensor integrated navigation systems*. London, UK: Artech house.2013. pp. 559-615.
- [46] EU-US Cooperation on Satellite Navigation Working Group C, "ARAIM Technical Subgroup Milestone 2," February 11, 2015. [Online] Available: <https://www.gps.gov/policy/cooperation/europe/2015/working-group-c/>.
- [47] W. Wen, L.T. Hsu, & G. Zhang, "Performance Analysis of NDT-based Graph SLAM for Autonomous Vehicle in Diverse Typical Driving Scenarios of Hong Kong," *Sensors*, 18(11), 3928.
- [48] X. Bai, W. Wen, L.T. Hsu, "Robust Visual-Inertial Integrated Navigation System Aided by Online Sensor Model Adaption for Autonomous Ground Vehicles in Urban Areas," DOI: 10.20944/preprints202003.0018.v1. Mar. 2020.
- [49] R. Merwe, E.A. Wan, "Sigma-point Kalman filters for integrated navigation," In *Proceedings of the 60th Annual Meeting of the Institute of Navigation (ION) 2004*, Dayton, USA, Jun. 2004, pp. 641-654.
- [50] B. Cui, X. Wei, X. Chen, J. Li, L. Li. "On sigma-point update of cubature Kalman filter for GNSS/INS under GNSS-challenged environment," *IEEE Transactions on Vehicular Technology*. vol. 68, no. 9, pp. 8671-8682. Jul. 2019.
- [51] X. Tang, G. Falco, E. Falletti, L.L. Presti, "Theoretical analysis and tuning criteria of the Kalman filter-based tracking loop," *GPS Solutions*, vol. 19, no. 3, pp. 489-503, Jul. 2015.
- [52] L.T. Hsu, "Analysis and modeling GPS NLOS effect in highly urbanized area," *GPS solutions*, vol. 22, no. 1, pp. 7, Jan. 2018.
- [53] T. G. Reid, S.E. Houts, R. Cammarata, *et al.*, "Localization Requirements for Autonomous Vehicles," *SAE International Journal of Connected and Automated Vehicles*, vol. 2019, no. 2, pp. 173-190, 2019.
- [54] T. Walter, K. Gunning, R. Phelts, and J. Blanch, "Validation of the unfaulted error bounds for ARAIM," *NAVIGATION: Journal of the Institute of Navigation*, vol. 65, no. 1, pp.117-133. Mar. 2018.